

INITIAL RESULTS OF A PASSIVE MILLIMETER-WAVE IMAGER USED FOR CONCEALED WEAPON DETECTION BHU-2D-U

Cheng Zheng*, Xianxun Yao, Anyong Hu, and Jungang Miao

School of Electronic and Information Engineering, Beihang University, 37th Xueyuan Road, Haidian District, Beijing 100191, China

Abstract—A passive millimeter-wave imager BHU-2D-U has been developed by Beihang University. This imager is designed for detecting concealed weapons on human body. It is a subsequent model of BHU-2D, which is also developed by the same group. In this paper, the improvements of BHU-2D-U over BHU-2D are introduced. Firstly, BHU-2D-U is used for whole body scan, which is different from BHU-2D. Thus, the field of view (FOV) of the new imager is enlarged and a new antenna array type is adopted. Secondly, the enlarged FOV requires smaller antenna spacing and compact receiver arrays. In order to reduce the volume of the receivers, I/Q demodulators operating in double side band mode are adopted because it does not need the image-reject filter, which is usually a bulky one. Thirdly, the quantity of the correlators increases because the number of receiving elements is doubled. To cope with the increase of the correlator quantity, a multiplexing technique is used in the FPGA internal layout of the correlator array unit. After a brief introduction, the system design and configuration is illustrated in detail. Finally, imaging experiments on a person with concealed weapon are conducted, by which the design and image reconstruction algorithms are verified. To conclude, initial results of BHU-2D-U have proved that the improvements are effective.

1. INTRODUCTION

Passive millimeter-wave (mmW) imagers have become a very effective and attractive approach in concealed weapon detection applications because their inherent ability to detect objects under the clothing of

Received 28 June 2013, Accepted 2 September 2013, Scheduled 5 September 2013

* Corresponding author: Cheng Zheng (zhengcheng@sina.com).

a person [1–9]. Passive imagers do not emit electromagnetic energy. They receive the spontaneous radiation emitted or reflected by the subject of interest. Therefore, passive mmW imagers are safe for the

Table 1. Comparison between BHU-2D-U and BHU-2D.

Parameter	BHU-2D-U	BHU-2D
Center Frequency	34.0 GHz	34.1 GHz
Receiver Bandwidth	400 MHz	160 MHz
LO Frequency	32 GHz (used for RF front end) 2 GHz (used for I/Q demodulator)	
Field of View	22° (horizontal) 40° (vertical)	20° (circular FOV)
Synthetic Beamwidth	1.4° (horizontal) 1.2° (vertical)	1.1°
Temperature Sensitivity	~1.0 K (1 s integration time)	~0.7 K (1 s integration time)
Geometry of Antenna Array	U-shaped	Y-shaped
Number of Receiving Elements	48	24
Antenna Element Spacing	2.62 λ (horizontal) 1.46 λ (vertical)	3.07 λ
Number of Baselines	1267	427
Receiver Type	Dual conversion (DSB for I/Q demodulator)	Dual conversion (SSB for I/Q demodulator)
Number of Correlators	2704 (2676 is effective)	924
Number of Cross Correlators	2560 (2532 is effective)	852
Power Measurement System	8 bit ADC and auto correlator	Statistical power measurement method [15]
Calibration	Noise Injection (External Point Source) Background Cancellation	

human body. However, the image quality of these instruments is often limited by low-level signal to noise ratio (SNR). Thus, they usually requires long integration time, which makes the capturing speed a very critical issue. Synthetic aperture interferometric radiometer (SAIR) has been proved to be an effective technique to provide the high imaging rate and large field of view (FOV) required in security applications [10–13].

A two-dimensional SAIR BHU-2D-U used for concealed weapon detection has been developed in Beihang University. BHU-2D-U is an improved model of BHU-2D [14], which has validated the design principle and imaging reconstruction algorithm. The comparison between BHU-2D-U and BHU-2D is shown in Table 1. The main goal of the improvements over the old model is to increase the FOV to meet the requirements of whole human body scan in security applications. For BHU-2D, the FOV is a circular in shape. When a person stands in front of the instrument and the distance between them is 3 m, the effective imaging area is about 1 m in width and 1 m in height, which is not enough for whole human body scan. Practically, 1 m in width and 2 m in height are usually required, which corresponds to a rectangular FOV of $19^\circ \times 37^\circ$. To preserve some margin, $22^\circ \times 40^\circ$ is used in the final. To obtain the rectangular FOV, different element spacings are required along the horizontal and vertical orientation. Thus, a U-shaped array is used in the new model named BHU-2D-U. Since the FOV along vertical orientation is about two times larger than BHU-2D, the element spacing becomes smaller, which requires smaller receiving elements. In order to reduce the dimensions of the receiving elements, I/Q demodulators operating in double side band (DSB) mode are adopted because it does not need the image-reject filter, which is usually a bulky one. The smaller element spacing also leads to an increasing in correlator quantity, as shown in Table 1. In order to cope with the problem, a multiplexing technique is used in the internal layout of the field programmable gate array (FPGA).

In this article, the system design, configuration and some initial experiment results of BHU-2D-U are presented.

2. SYSTEM DESIGN

2.1. Imaging Principle Review

The principle of SAIR is to measure the spectral components of the brightness temperature distribution in the FOV by microwave interferometry. Each pair of antennas in the SAIR can be seemed as an interferometer. Figure 1 shows a block diagram of a single interferometer. By measuring the complex cross-correlation of the

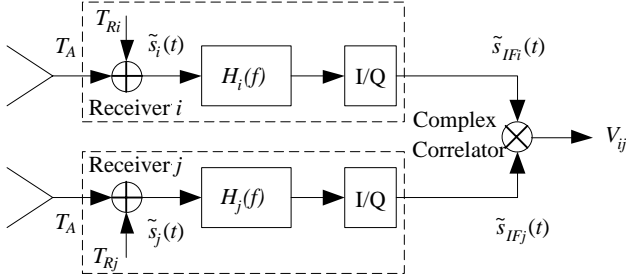


Figure 1. Block diagram of a single interferometer.

signals $\tilde{s}_i(t)$ and $\tilde{s}_j(t)$ collected by the pair of antennas i and j , the so-called visibility function or spatial frequency V_{ij} can be obtained [16]

$$\begin{aligned}
 V_{ij}(u, v) &= \frac{1}{k_B \sqrt{B_i B_j} \sqrt{G_i G_j}} \cdot \frac{1}{2} \langle s_i(t) s_j^*(t) \rangle \\
 &= \frac{1}{\sqrt{\Omega_i \Omega_j}} \iint_{\xi^2 + \eta^2 \leq 1} \frac{T_B(\xi, \eta)}{\sqrt{1 - \xi^2 - \eta^2}} F_{ni}(\xi, \eta) \\
 &\quad \cdot F_{nj}^*(\xi, \eta) \tilde{r}_{ij} \left(-\frac{u_{ij}\xi + v_{ij}\eta}{f_0} \right) e^{-j2\pi(u\xi + v\eta)} d\xi d\eta \quad (1)
 \end{aligned}$$

where $k_B = 1.38 \times 10^{-23} \text{ J} \cdot \text{K}^{-1}$ is the Boltzmann's constant and (u, v) the vector between the two antennas in wavelength, which is usually called baseline. $B_{i,j}$ and $G_{i,j}$ are the noise bandwidth and power gain of the receiving elements, respectively. $\Omega_{i,j}$ and $F_{ni,nj}(\xi, \eta)$ are the equivalent solid angle and normalized radiation voltage patterns of the antennas. $\xi = \sin(\theta) \cos(\varphi)$ and $\eta = \sin(\theta) \sin(\varphi)$ are the direction cosines in spherical coordinate system. T_B is the brightness temperature of the target. f_0 is the center frequency of the receivers. $\tilde{r}_{ij}(-\tau)$ is fringe washing function (FWF) and can be expressed as

$$r_{ij}(\tau) = \int_0^\infty H_{ni}(f) H_{nj}^*(f) e^{j2\pi f\tau} df \quad (2)$$

where $H_{ni}(f)$ and $H_{nj}(f)$ are the normalized frequency responses of the two receivers. Usually, $H_{ni}(f)$ is almost the same as $H_{nj}(f)$ and $\tilde{r}_{ij}(-\tau)$ can be approximated by 1 [16]. Consequently, $T_B(\xi, \eta)$ could be reconstructed by calculating the Inverse Fourier Transform (IFT) of the visibilities based on Equation (1).

Equation (1) is an integral form of the imaging principle. Practically, each pair of the antennas in the array composes a baseline and the visibility function $V(u, v)$ corresponding to the baseline can be measured. Consequently, the visibility function is sampled by

the antenna array. When the sampling spacing does not meet the Nyquist Theorem, aliasing error will be introduced in the SAIR system. Generally, the anti-aliasing FOV along ξ or η axis could be expressed as

$$\theta_{\max} = 2 \arcsin(1/d - 1) \quad (3)$$

where d in wavelength is the spacing between visibility function samples along axis u or v . Figure 2 shows the relationship between the sampling spacing and the anti-aliasing FOV. As it is shown, $d < 1$ is required to guarantee an anti-aliasing FOV. On the other hand, the angular resolution in this condition could be expressed as [17]

$$\Delta\xi \approx \frac{\pi\lambda}{4\rho_{\max}} \approx 0.8 \frac{\lambda}{\rho_{\max}} \quad (4)$$

where ρ_{\max} is the largest baseline along u or v direction and λ the wavelength corresponding to the center frequency of the receiver. Therefore, for a required angular resolution and FOV, Equation (3) requires a small spacing between visibility samples while Equation (4) requires large coverage of the spatial frequency. For BHU-2D-U, the FOV is about $22^\circ \times 40^\circ$ and the resolution is about 1.4° , which requires about 115 receiving elements and more than 10000 cross correlators. Since there are too many visibility function samples in this scheme, the complexity will be very high. To reduce the complexity and cost of the imager, background cancellation method is used in BHU-2D-U. This method is used to reduce the influence of the aliasing error caused by under sampling of the visibility function. For a given d , the anti-aliasing FOV with background cancellation is [14]

$$\theta_{\max}^{\text{BC}} = 2 \arcsin(1/2d) \quad (5)$$

As it is shown in Figure 2, the anti-aliasing FOV with background cancellation is expanded for a given d . However, when background cancellation is applied, the visibility function samples need to be pre-processed before image reconstruction. The pre-processed visibility function sample is

$$V_{\text{norm}}(u, v) = \frac{V_T(u, v) - V_B(u, v)}{V_C(u, v) - V_B(u, v)} \quad (6)$$

where $V_T(u, v)$ is the visibility of the target, $V_B(u, v)$ the visibility of the background, and $V_C(u, v)$ the visibility of a calibration point source. With background cancellation method, the requirement of d is reduced. For BHU-2D-U, 48 receiving elements and 2532 cross correlators are required, which is simpler than the scheme of 115 receiving elements.

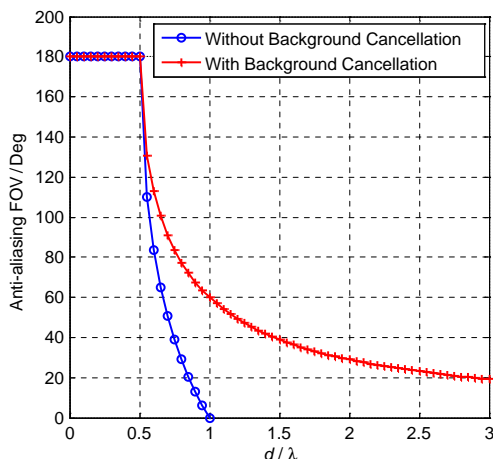


Figure 2. The anti-aliasing FOV of the SAIR with/without background cancellation.

2.2. Antenna Array of BHU-2D-U

Based on background cancellation method, the antenna array of BHU-2D-U is designed. There are 48 receiving elements in BHU-2D-U and they are installed on a plane in U-shaped geometry. The U-shaped configuration is adopted because it can provide different visibility sample spacings along axis u and v , which leads to a rectangular FOV fitting for the application of concealed weapon detection.

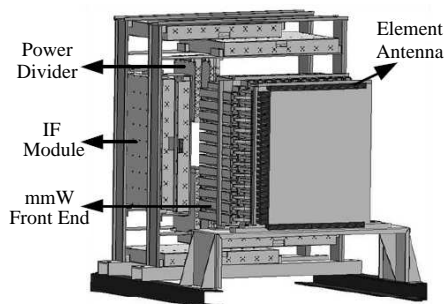


Figure 3. Antenna array of BHU-2D-U.

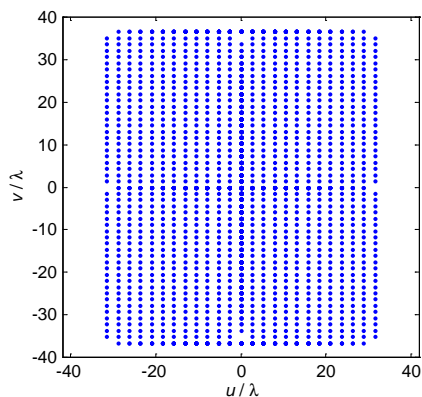


Figure 4. Distribution of visibility function samples.

Figure 3 shows the configuration of the array. There are three arms in the array, including two horizontal arms and one vertical arm. The horizontal arm contains 12 receiving elements and the spacing between elements is 2.62λ , while the vertical arm contains 24 receiving elements and the spacing is 1.46λ . The distribution of the visibility function samples are illustrated in Figure 4. There are 1267 unique baselines in the system. The largest baseline of the instrument is 31.45λ and 36.55λ along horizontal and vertical orientations, respectively, which lead to a resolution of $1.4^\circ \times 1.2^\circ$.

3. INSTRUMENT DESCRIPTION

3.1. System Configuration

A block diagram of BHU-2D-U is illustrated in Figure 5. The instrument consists of 48 receiving elements located in a U-shaped geometry. Each element is composed of a pyramid horn and a dual-conversion receiver with I/Q demodulator. Coherent LOs are generated by a frequency synthesizer and fed into receivers through a group of dividers. Digital Signal Processing subsystem (DSP) computes the cross-correlations between the IF output signals of all receivers simultaneously and reconstruct the brightness temperature image.

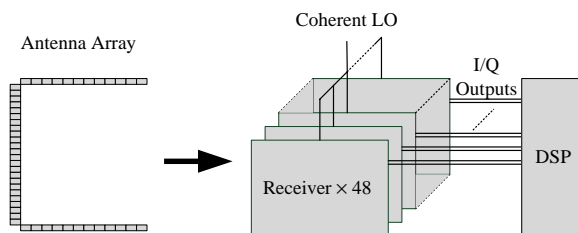


Figure 5. System configuration of BHU-2D-U.

3.2. Receiving Elements

Every receiving element in the antenna array is composed of an element antenna and a dual-conversion receiver. Figure 6 shows the block diagram of the receiving element.

In order to cover the rectangular and wide FOV, a pyramid horn is used as the element antenna for its simplicity. The outer dimension of the horn is $2.62\lambda \times 1.46\lambda$, which can make full use of the spacing between antennas and maximize the main beam efficiency. The -3 dB

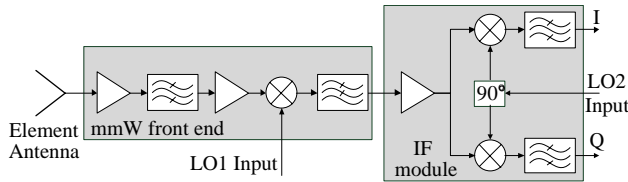


Figure 6. Block diagram of the receiving element.

beamwidth of the antenna is about $28^\circ \times 36^\circ$, which could be accepted for the requirements of $19^\circ \times 37^\circ$.

The signals collected by the antennas are fed into a group of dual-conversion receivers with I/Q demodulators. As it is shown in Figure 6, each receiver consists of a mmW front end and an IF module. The mmW front end converts the mmW signal into lower frequency signal, which will be then demodulated into I/Q outputs by the IF module. The first stage operates in single side band (SSB) mode for image rejection purpose, while the second stage operates in double side band (DSB) mode. DSB is used because the analytic signals is free from frequency image. Thus, it do not needs image-reject filter and results in lower receiver volume. The nominal gain and noise figure of the receivers are ~ 80 dB and ~ 4.2 dB respectively. In order to equalize the gain between channels, the gain of each IF module can be adjusted by a variable attenuator. The configuration of the receiver array is demonstrated in Figure 3. Since the dimension of the receiver cross section is $20\text{ mm} \times 20\text{ mm}$ and is larger than $1.46\lambda = 12.9\text{ mm}$, an interleaving method is adopted in the vertical arm.

3.3. Digital Signal Processing Subsystem

The I/Q outputs of the receivers are digitized and the complex correlations between signals are calculated in the DSP subsystem. Since the DSP subsystem contains 2676 correlators, for simplicity, 1 bit/2 level (1B/2L) correlators [18] are used. Considering 1B/2L correlator only gives the correlation coefficient of the input signals, the power of the input signals are measured to denormalize the coefficients into visibility function samples.

The block diagram of the DSP subsystem is illustrated in Figure 7. There are 96 data acquisition elements (DAEs) in the DSP. The quantization resolution is 8 bits to meet the requirements of power measurement units. After power measurement, the 8-bit data are converted into 1-bit data by comparators. In order to calibrate the offset errors of the ADCs, the average of the signals are estimated

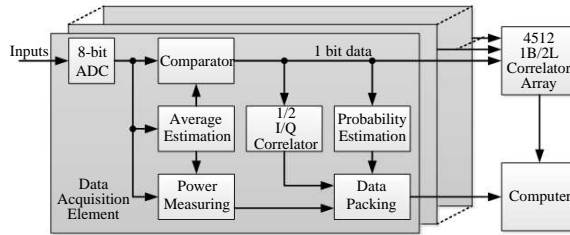


Figure 7. Block diagram of the DSP subsystem.

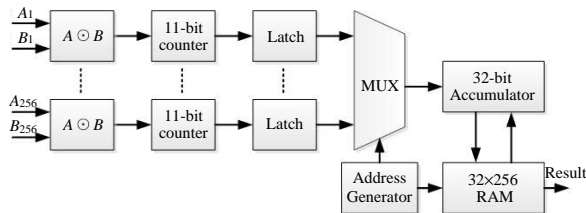


Figure 8. The FPGA internal layout of a correlator group.

and set as the thresholds of the comparators. After receiving the 1-bit data, the correlator unit computes the cross correlation coefficients with the 1-bit data. There are 2532 cross-correlators (4 correlators per baseline) in the unit. Besides, 144 additional correlations are calculated, including 48 correlations between I/Q outputs of one receiver as well as 96 correlations between the 1-bit data and artificial vectors of “all ones” (probability estimation). The former is used to calibrate the quadrature error [19], while the latter is required to calibrate the threshold errors of the comparators [20].

The 2532 cross correlators is implemented in a FPGA. Every 256 correlators are computed in a correlator group. Thus, there is 2560 correlators actually. Figure 8 shows the simplified block diagram of the FPGA internal layout. For BHU-2D-U, a typical integration time is about 0.1s~5s, which corresponds to a 31-bit counter in the 1B/2L correlator. In order to minimize the utilization of the configurable logic block (CLB), only the lower 11-bit counter is implemented with CLBs. The other bits are implemented by a RAM and an accumulator.

Finally, the measurements are collected, and then the visibility function samples could be calculated by the computer. By calculating the IFT of the visibility function samples, a brightness temperature image could be obtained in the computer. Figure 9 shows the structure of the DSP subsystem. Every Data Acquisition Unit (DAU) consists

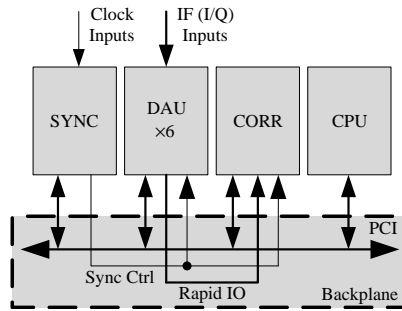


Figure 9. The structure of the DSP subsystem.

of 16 DAEs. The 1-bit data is transmitted to correlation array unit (CAU) by Rapid IO lanes and the cross correlation coefficients are calculated in the CAU. The SYNC unit is designed to synchronize CAU and DAUs. The DSP subsystem is installed in a standard 6U platform.

4. EXPERIMENTAL RESULTS

The components of BHU-2D-U have been developed and assembled at present, which is shown in Figure 10. In order to validate the design, imaging experiments on a point source and a person are conducted.

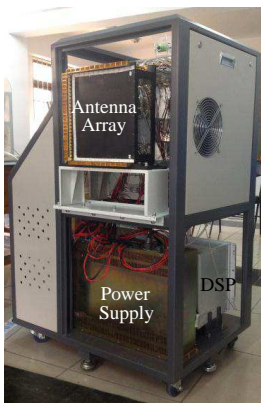


Figure 10. Photograph of the BHU-2D-U.

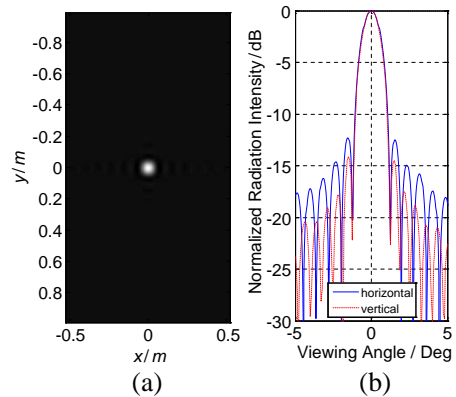


Figure 11. PSF of BHU-2D-U. (a) PSF of BHU-2D-U. (b) Cross-section of the PSF.

4.1. Imaging Result of a Point Source

The point source is located in front of the instrument and the distance between them is about 3 m. Since the solid angle subtended by the point source is smaller than the imaging resolution, the image of the point source can be interpreted as the point spread function (PSF) of the system. Figure 11(a) shows the result. In order to reduce the influence of the side lobe, Hanning window is applied before image reconstruction. Figure 11(b) shows the cross-section of the PSF, from which it could be seen that the angular resolution is about $1.3^\circ \times 1.3^\circ$, which is consistent with the design specification.

4.2. Imaging Result of a Person

Imaging experiment on a person is carried out. In order to form a uniform background, a metal plane with 45° incline to the ground is fixed behind the person. The plane can reflect the spontaneous radiation from the sky and form a uniform cold background. The integration time in the experiment is set to 0.5 s. The result is shown in Figure 12. The pictures shown on the left is captured by a camera and the corresponding imaging results are on the right. Figure 12(a) shows that the image obtained by BHU-2D-U matches the picture taken by the camera very well. It also can be seen that the brightness temperature distribution of a person is not uniform. It might be caused by the reflection of the environment. In Figure 12(b), a metal strip is held in the person's hand and it can be recognized clearly from the mmW image, although it is concealed under his shirt.

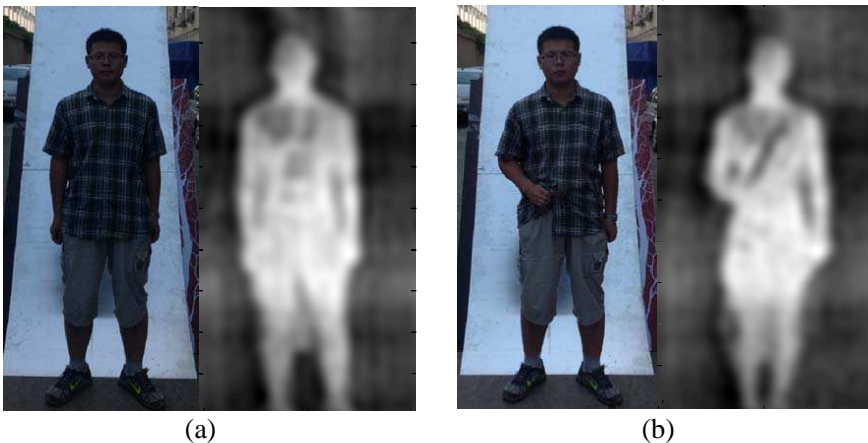


Figure 12. Imaging results of a person. (a) Imaging result of a person. (b) Imaging result of a person with concealed weapon.

5. CONCLUSION

The BHU-2D-U developed by Beihang University is an improved model of the passive mmW imager BHU-2D. It is designed to meet the requirements of the applications in whole human body scan at the security check point. In order to do so, a U-shaped antenna array is used, and some specification of the components is also modified. This article discusses the design and configuration of the instrument. Initial results of imaging experiments show that BHU-2D-U is capable of detecting concealed weapons.

REFERENCES

1. Wikner, D. A., "Progress in millimeter-wave imaging," *Proc. SPIE*, Vol. 7936, 79360D, Feb. 10, 2011.
2. Kolinko, V. G., S. Lin, A. Shek, W. Manning, C. Martin, M. Hall, O. Kirsten, J. Moore, and D. A. Wikner, "A passive millimeter-wave imaging system for concealed weapons and explosives detection," *Proc. SPIE*, Vol. 5781, 85–92, May 19, 2005.
3. Lovberg, J. A., C. Martin, and V. G. Kolinko, "Video-rate passive millimeter-wave imaging using phased arrays," *Proc. MWSYM*, 1689–1692, Honolulu, HI, Jun. 3–8, 2007.
4. Huang, J. and T. Gan, "A novel millimeter wave synthetic aperture radiometer passive imaging system," *Proc. ICMMT*, 414–417, Aug. 18–21, 2004.
5. Notel, D., J. Huck, S. Neubert, S. Wirtz, and A. Tessmann, "A compact mmW imaging radiometer for concealed weapon detection," *Proc. IRMMW-THz*, 269–270, Cardiff, Sep. 2–9, 2007.
6. Williams, T. D. and N. M. Vaidya, "A compact, low-cost, passive mmW security scanner," *Proc. SPIE*, Vol. 5789, 109–116, May 19, 2005.
7. Kim, W., N. Moon, Y. Chang, M. Lee, S. Jung, J. Choi, J. Jung, and Y. Kim, "System design of focal plane array based millimeter-wave imaging radiometer for concealed weapon detection," *Proc. IGARSS*, 2258–2261, Vancouver, BC, Jul. 24–29, 2011.
8. Lee, H., D. Lee, S. Yeom, J. Son, V. P. Guschin, and S. Kim, "Passive millimeter wave imaging and analysis for concealed object detection," *Proc. ICMiA*, 98–101, Macao, Oct. 24–26, 2011.
9. Doghri, A., A. Ghiotto, T. Djerafi, and K. Wu, "Early demonstration of a passive millimeter-wave imaging system using substrate integrated waveguide technology," *Proc. MMS*, 215–218, Hammamet, Sep. 8–10, 2011.

10. Salmon, N. A., J. Beale, A. Beard, M. Dean, S. Hayward, P. Hickling, S. T. Chiw, H. Ghafouri-Shiraz, P. Hall, R. Macpherson, R. Lewis, A. H. Lettington, and D. Dunn, "An all electronic passive millimetre wave imaging system," *Proc. SPIE*, Vol. 5789, 11–15, May 19, 2005.
11. Salmon, N. A., J. Beale, and S. Hayward, "Compact and lightweight digital beam-forming passive millimeter imagers," *Proc. SPIE*, Vol. 7117, 711709, Oct. 2, 2008.
12. Salmon, N. A., R. Macpherson, A. Harvey, P. Hall, S. Hayward, P. Wilkinson, and C. Taylor, "First video rate imagery from a 32-channel 22-GHz aperture synthesis passive millimetre wave imager," *Proc. SPIE*, Vol. 8188, 818805, Oct. 6, 2011.
13. Salmon, N. A., P. N. Wilkinson, C. T. Taylor, and M. Benyazzar, "Minimising the costs of next generation aperture synthesis passive millimetre wave imagers," *Proc. SPIE*, Vol. 8188, 818808, Oct. 6, 2011.
14. Zheng, C., X. Yao, A. Hu, and J. Miao, "A passive millimeter-wave imager used for concealed weapon detection," *Progress In Electromagnetics Research B*, Vol. 46, 379–397, 2013.
15. Zheng, C., X. Yao, A. Hu, and J. Miao, "Statistical power measurement unit for an 8 MM-band two dimensional synthetic aperture interferometric radiometer BHU-2D," *Progress In Electromagnetics Research M*, Vol. 27, 119–128, 2012.
16. Corbella, I., A. Camps, F. Torres, and J. Bara, "Analysis of noise-injection networks for interferometric-radiometer calibration," *IEEE Trans. Geosci. Remote Sens.*, Vol. 48, No. 4, 545–552, Apr. 2000.
17. Camps, A., "Application of interferometric radiometry to earth observation," Chapter 3, Ph.D. Dissertation, Polytechnic University of Catalonia, Spain, 1996.
18. Ruf, C. S., "Digital correlators for synthetic aperture interferometric radiometry," *IEEE Trans. Geosci. Remote Sens.*, Vol. 33, No. 5, 1222–1229, Sep. 1995.
19. Corbella, I., F. Torres, A. Camps, A. Colliander, M. Martín-Neira, S. Ribo, K. Rautiainen, N. Duffo, and M. Vall-llossera, "MIRAS end-to-end calibration: Application to SMOS L_1 processor," *IEEE Trans. Geosci. Remote Sens.*, Vol. 43, No. 5, 1126–1134, May 2005.
20. Zheng, C., X. Yao, A. Hu, and J. Miao, "Closed form calibration of 1 bit/2 level correlator used for synthetic aperture interferometric radiometer," *Progress In Electromagnetics Research M*, Vol. 29, 193–205, 2013.